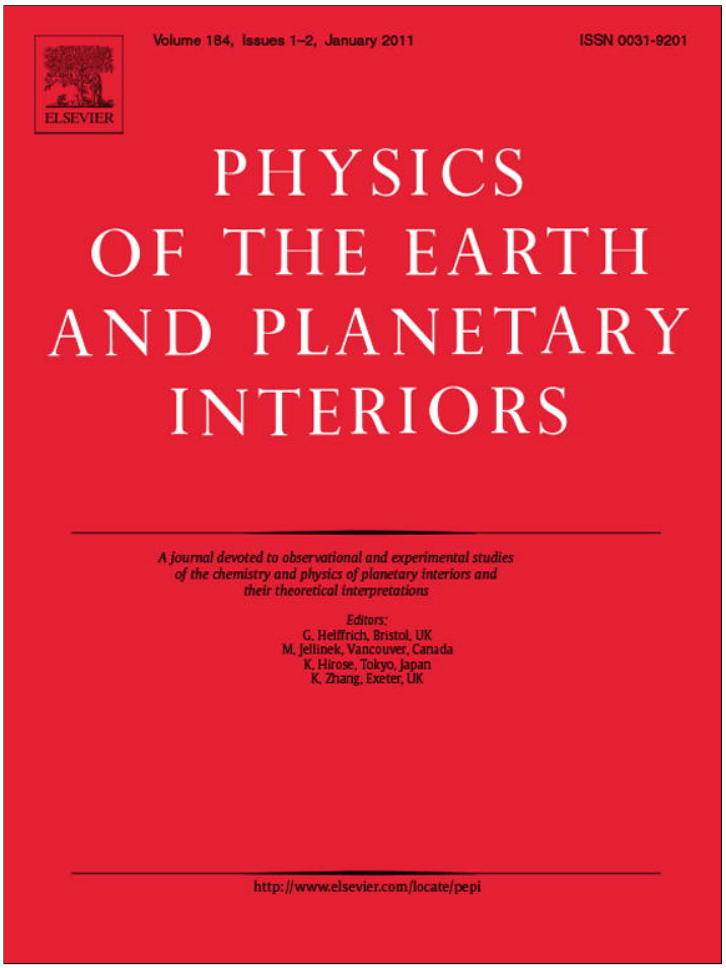

Physics of the Earth and Planetary Interiors 184 (2011) 51–62

Contents lists available at ScienceDirect

Physics of the Earth and Planetary Interiors

journal homepage: www.elsevier.com/locate/pepi

Influence of variable uncertainties in seismic tomography models on constraining mantle viscosity from geoid observations

Choon-Ki Lee[a,b], Shin-Chan Han[a,b,*], Bernhard Steinberger[c,d,e]

[a] Planetary Geodynamics Laboratory, Code 698, NASA Goddard Space Flight Center, Greenbelt, MD, USA
[b] Goddard Earth Science and Technology Center, University of Maryland at Baltimore County, Baltimore, MD, USA
[c] Helmholtz Centre Potsdam, GFZ German Research Centre for Geosciences, Telegrafenberg, 14473 Potsdam, Germany
[d] Physics of Geological Processes and Geosciences, University of Oslo, Oslo, Norway
[e] Centre for Advanced Studies, Norwegian Academy of Sciences and Letters, Drammensveien 78, NO-0271, Oslo, Norway

ARTICLE INFO

Article history:
Received 31 March 2010
Received in revised form 14 October 2010
Accepted 15 October 2010

Edited by: Mark Jellinek.

Keywords:
Mantle viscosity
Geoid
Seismic tomography
Total least squares

ABSTRACT

The radial viscosity structure of the Earth is explored on the basis of the geoid observations. The variations of uncertainty in seismic tomography models are accounted for when finding the radial viscosity structure. The new methodology we propose attempts to fit more closely those features of the geoid that are better constrained by tomography models and avoids to fit those features that are poorly constrained. This approach is particularly important because the error of geoid predictions caused by uncertainties in seismic tomography models is overwhelmingly larger than the noise in the geoid measurements. The synthetic tests indicate that the viscosity structures obtained by disregarding the uncertainty variations in seismic tomography models can be biased depending on the geoid spectral band and on the 'input' seismic tomography model. When the uncertainty variations in seismic models are considered in the inversion process, results do not indicate a viscosity in the transition zone lower than in the upper mantle. A robust feature found with the new method is a viscosity in the upper mantle two orders of magnitude smaller than in the lower mantle. The error covariance of seismic tomography models is critical for the method we suggest. A covariance matrix rigorously derived by seismologists should help to even more reliably infer the viscosity structure and relation between anomalies in density and seismic velocities from surface observations such as the geoid, and thus lead to a better knowledge of the Earth interior.

1. Introduction

It is an intriguing observation that the seismically-inferred density structure and the observed gravity field from satellites are anti-correlated (Dziewonski et al., 1977). The fluid mechanical models introduced by Hager and O'Connell (1981) and Richards and Hager (1984) indicate that the mantle flow caused by the density contrast often contributes more to the geoid anomaly than the density contrast itself by yielding a dynamically maintained deformation at the density interfaces (i.e., dynamic topography). The radial structure of mantle viscosity of the Earth is a key parameter to control dynamic topography and thus can be inferred from the global observations of geoid and gravity anomalies. Various studies considering also post-glacial rebound data (Forte and Mitrovica, 1996; Mitrovica and Forte, 2004), mineral physics (Steinberger and Calderwood, 2006), and the effects of lateral viscosity variation (Richards and Hager, 1989; Zhang and Christensen, 1993; Paulson et al., 2005; Kaban et al., 2007; Moucha et al., 2007; Tosi et al., 2009) have been carried out to constrain mantle viscosity structure. Hager and Richards (1989), Ricard et al. (1989), and King (1995), to name a few, conclude a gradual increase in viscosity from upper mantle to lower mantle. Ricard et al. (1989), King and Masters (1992), and Soldati et al. (2009) show a transition zone less viscous than the uppermost mantle by two or three orders of magnitude suggesting a viscosity decrease due to the softening of transition zone minerals related to high water content and phase change.

The uncertainty in radial mantle viscosity inferred from the geoid observations stems from a difficulty in modeling appropriate surface boundary conditions (Thoraval and Richards, 1997), compressibility of the mantle (Forte and Peltier, 1991; Panasyuk et al., 1996), possible chemical layering and phase transitions (Wen and Anderson, 1997; Čadek et al., 1998), lateral viscosity variations (LVV), etc. Furthermore, the uncertainty associated with the a priori assumption of the Earth's density structure, which is derived mostly from seismic (velocity) tomography models and a velocity-to-density conversion factor, is critical, because the Earth's

* Corresponding author at: Planetary Geodynamics Laboratory, Code 698, NASA Goddard Space Flight Center, Greenbelt, MD, USA.
E-mail address: shin-chan.han@nasa.gov (S.-C. Han).

0031-9201/$ – see front matter © 2010 Elsevier B.V. All rights reserved.
doi:10.1016/j.pepi.2010.10.012

density anomalies are used typically as "model constants" in geoid computation.

In most inversion studies including the literature introduced above, the analysis has been formulated without explicitly considering uncertainty in the seismic tomography model. The inversion is performed such that the solution yields the best fit to the geoid observations, typically in terms of variance reduction, i.e., in a least squares sense. Here we consider the uncertainty in the density structure with the "total least squares" (TLS) approach in order to obtain unbiased viscosity solutions and compare with the results from the least square (LS) method. We present an alternative misfit function between the observations and model predictions explicitly considering the uncertainty in the seismic tomography models. The effects of the model parameter uncertainty on the viscosity solutions are highlighted.

2. Geoid model

A fluid mechanical model for the geoid is derived by implementing mass conservation (continuity equation), momentum conservation (equation of motion), and Poisson's equation. The solution can be written in the integral form with the input density anomaly (driving force of the flow) and so-called 'geoid kernels' as follows:

$$N_{lm} = \frac{3}{2l+1}\frac{1}{\bar{\rho}}\int_{R_{CMB}}^{R_E} \delta\rho_{lm}(r) G_l(r) dr, \quad (1)$$

where N_{lm} is non-hydrostatic geoid of degree l and order m, $\delta\rho_{lm}(r)$ is the density anomaly, $G_l(r)$ is the geoid kernel (a non-linear function of viscosity structure), $\bar{\rho}$ is the average density of the Earth, R_E is the radius of the Earth, and R_{CMB} is the radius of the core-mantle boundary (CMB). The analytic expression of $G_l(r)$ for the two-layered viscosity structure is given in Forte and Peltier (1987) and semi-analytic solutions are provided for more general cases in Hager and Richards (1989). The density anomaly $\delta\rho_{lm}(r)$ is obtained typically from the seismic tomography (velocity) model using a scaling factor ζ, which needs to be determined as well, and which relates velocities to densities through

$$\delta \ln \rho(r) = \zeta(r)\delta \ln V_s(r). \quad (2)$$

3. Viscosity structure minimizing the least-square error norm

With the geoid observations, we find the best-fit viscosity structure by computing multiple forward models with various sets of the viscosity parameters. The radial Earth model for viscosity consists of four viscous layers denoting lithosphere (0–100 km), upper mantle (100–400 km), transition zone (400–670 km), and lower mantle (670–2891 km). Since only relative changes of viscosity can be inferred from the geoid observations, the value of viscosity in the lower mantle is set to be 10^{22} Pa s in our study. For other layers, we prescribe a plausible range of variations within three orders of magnitude and establish an equidistant model parameter grid. We use the non-hydrostatic geoid observations from GRACE (Gravity Recovery And Climate Experiment) gravity model GGM02S (Tapley et al., 2005).

First, we calculate the (forward) geoid models for the predefined model parameter space using Eq. (1) and then, in the context of the least-squares minimization, the misfit between the model and observed geoid is evaluated by computing the sum of the squared residuals as follows:

$$\psi(\mathbf{h}) = \sum_{l=l_{\min}}^{l_{\max}} \sum_{m=-l}^{l} \left(N_{lm}^{\text{obs}} - N_{lm}^{\text{mod}}(\mathbf{h})\right)^2, \quad (3)$$

where N_{lm}^{mod} and N_{lm}^{obs} are the spherical harmonic coefficients of the modeled and observed geoid, respectively. $\mathbf{h}$ describes the viscosity parameter used in the forward computation. $\psi(\mathbf{h})$ is essentially equivalent to the square of the geoid difference integrated over the globe. For the density model, we test six S-wave tomography models including s20rts (Ritsema and van Heijst, 2000), sb4l18 (Masters et al., 1999), saw24b16 (Mégnin and Romanowicz, 2000), s362d1 (Gu et al., 2001), ngrand (Grand, 2002), and s20a (Ekström and Dziewonski, 1998). The comparison and summary for each model is given in Becker and Boschi (2002).

In general, as shown in Fig. 1, the best-fitting viscosity structures from six tomography models and GRACE geoid observations in degrees from 2 to 12 agree with the viscosity profiles obtained from Ricard et al. (1989), King and Masters (1992), and more recently Soldati et al. (2009). The results place the lowest viscosity in the transition zone between 400 and 670 km and show a two orders of magnitude larger viscosity in the lower mantle. However, the geoid observations seem to be insensitive to the lithosphere viscosity further as long as it is less than lower mantle viscosity, as shown in Fig. 1(b). Also there is a trade-off between lithosphere and upper mantle viscosity. To avoid the ambiguity of the viscosity solutions caused by less sensitivity to lithosphere viscosity, we fix the lithosphere viscosity to be the same as the lower mantle viscosity. Therefore, the parameters in our analysis will be the transition zone viscosity (η_{TZ}) and the upper mantle viscosity (η_{UM}) relative to the lower mantle viscosity.

4. Influence of uncertainty in seismic tomography models on viscosity solutions

The seismic tomography models we use show a discrepancy in velocity perturbation as a function of depth, as shown in Fig. 2(a). The models consist of spherical shells in which lateral velocity variations with respect to the preliminary reference Earth model (PREM) (Dziewonski and Anderson, 1981) are expanded with spherical harmonic coefficients. For consistency in comparison, we evaluate each model at the same depths (total 20 discrete layers) following the radial parameterization of the SMEAN tomography model (Becker and Boschi, 2002).

The velocity variations derived by seismic methods are mainly related to temperature changes (Karato, 1993) but also dependent on changes in material composition, for example, in the vicinity of the melting zone (Sato et al., 1989). Although density is linearly related to temperature by thermal expansion, density is more sensitive to changes in the composition than seismic velocity is (Jordan, 1978). This yields a difficulty in deriving the density structure from seismic velocity. As a reference velocity-to-density scale factor (DSF) profile for this analysis, we use one of the thermal scaling profiles determined by Simmons et al. (2007), denoted DSF6 in Fig. 2(b). Other simple scale profiles including uniform scale factors are considered as well and shown in Fig. 2(b).

The geoid signal in the lowest degrees 2 and 3 is strongly affected by the density variations in the lowermost part of the mantle. The structures in the shallower regions are more responsible for the geoid in the intermediate degrees from 4 to 12 or so, because the geoid kernels for the intermediate degrees have the largest values in the upper mantle and the transition zone, in general. We perform the viscosity optimization in the four spectral bands l = 2–12, l = 4–12, l = 6–12, and l = 8–12. Using six tomography models and six DSF's as shown in Fig. 2, we find the viscosity profiles which give the minimum norm value defined in Eq. (3) from the GRACE geoid. In each band, the viscosity solutions look similar regardless of tomography models and scale factor profiles (Fig. 3). However, the solutions significantly differ depending on the spectral bands of the geoid data used in the analysis. For the spectral band l = 2–12, the

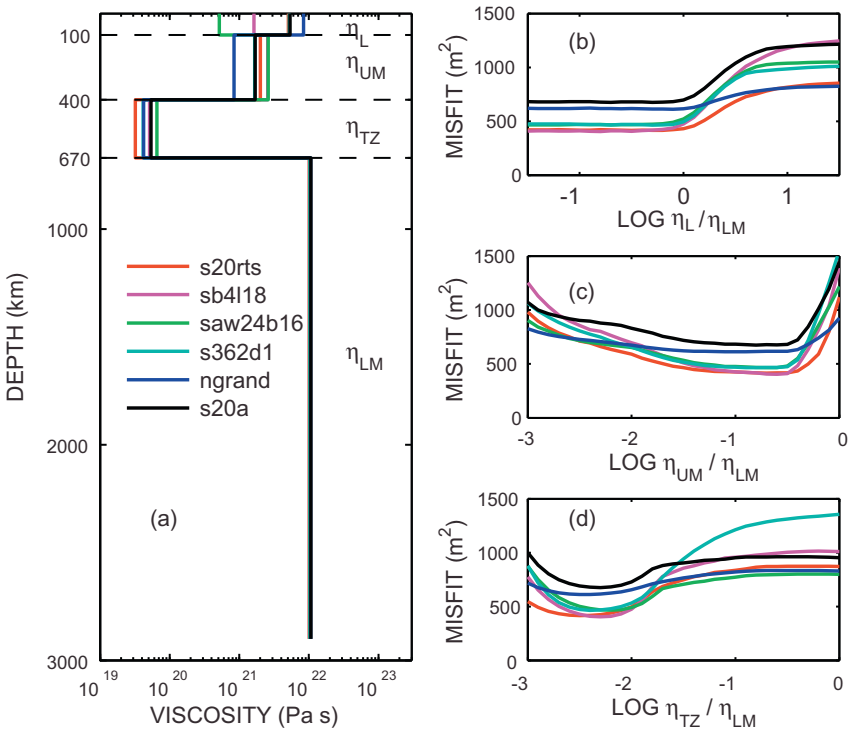

Fig. 1. (a) Radial viscosity structures inferred from geoid observations with six seismic (S-wave velocity) tomography models. The viscosity of lithosphere (η_L), upper mantle (η_{UM}), and transition zone (η_{TZ}) relative to the fixed viscosity of the lower mantle ($\eta_{LM} = 10^{22}$ Pa s) are determined by fitting the theoretical model to the GRACE non-hydrostatic geoid. (b) Variation of the misfit between model and observed geoid with the change in lithosphere viscosity. (c) and (d) as for (b) but the change in upper mantle viscosity and in transition zone viscosity, respectively.

resulting viscosity profile is similar to the models from other studies such as Ricard et al. (1989), King and Masters (1992), and Soldati et al. (2009), for example, with the lowest viscosity in the transition zone. On the contrary, the viscosity profiles for the highest spectral band $l = 8$–12, which may be sensitive to lateral viscosity variation, yield the lowest viscosity in the upper mantle. This lowest viscosity in the upper mantle can be found in the previous studies analyzing the spherical harmonics of $l = 7$–12 (Kogon and McNutt, 1993) and of $l = 12$–25 (Kido et al., 1998). We find that a lithosphere viscosity lower than the upper mantle viscosity helps to reduce the

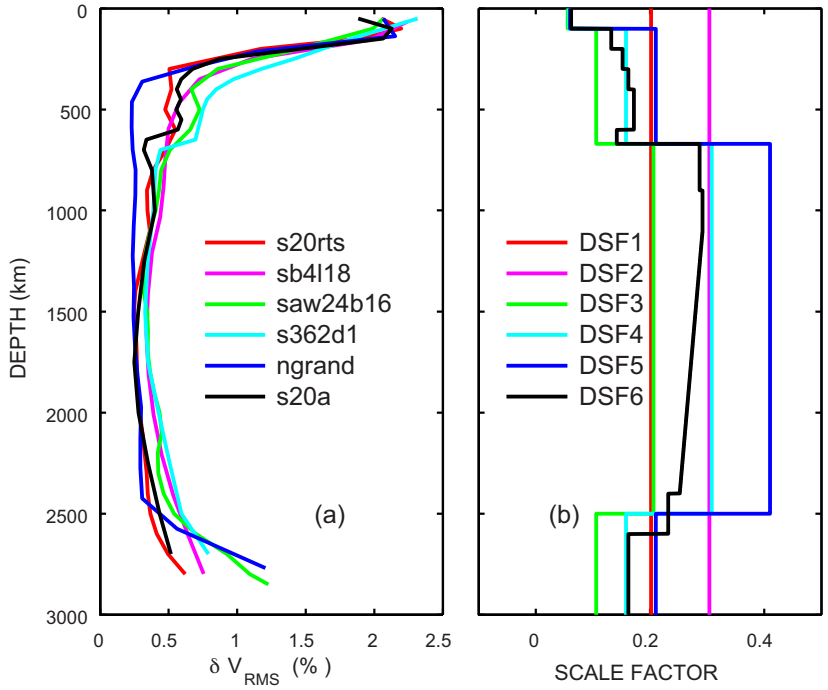

Fig. 2. (a) Radial RMS variation of seismic velocity perturbations for six tomography models. The velocity variations indicate the relative deviation from PREM. (b) Velocity-to-density scale factor (DSF) profiles tested in this study. The profile DSF6 is used as a reference scale factor.

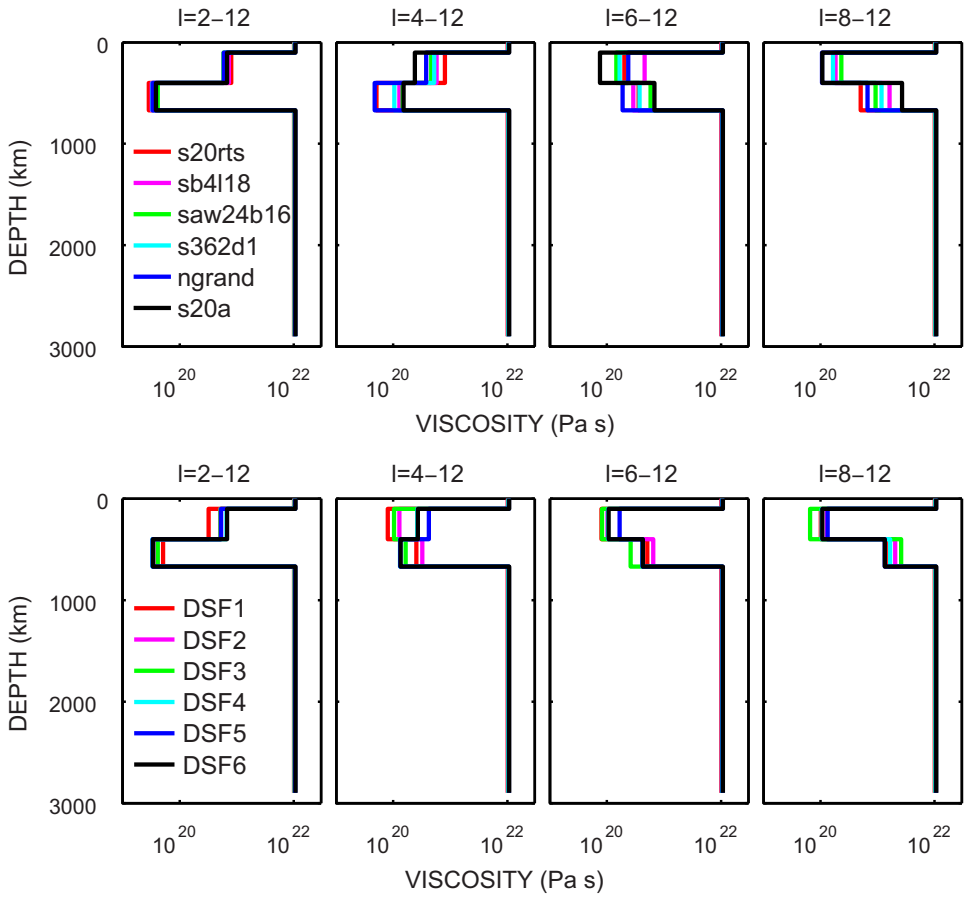

Fig. 3. Best-fitting viscosity profiles for different tomography models but the same scale factor profile DSF6 (upper panels) and for different scale factor profiles but the same (mean) tomography model (lower panels), for four cases of the geoid spectral band. The lithosphere viscosity is set to be the same as in the lower mantle.

inconsistency of the viscosity solutions dependent on the spectral band of the geoid observations. However, a lower viscosity in the lithosphere contradicts the estimates of effective viscosity based on the ratio of shear stress to strain rates (Gordon, 2000).

Our speculation is that the variations of errors in tomography models (as a function of depth and spherical harmonic degree) can lead to such inconsistency among the viscosity solutions. To verify this hypothesis, we perform simulations using synthetic data. First, we make a mean tomography model by taking the average of six models and compute the synthetic geoid for a given viscosity profile. The mean tomography model and the given viscosity profile are assumed to be 'true' velocity and viscosity structure of the Earth, respectively. Second, we prepare a number of noisy tomography models by means of adding random noise to the mean tomography model. The random noise is determined from the error covariance of tomography models. Since the covariance is typically unknown (or not provided), we take the 'empirical' covariance computed from six tomography models. For simplicity, the covariance of six models is evaluated for each spherical harmonic coefficient. We assume the spherical harmonic coefficients in each layer (spherical shell) are not correlated, but the spherical harmonic coefficients of the same degree and order in different layers are correlated. Because the tomography models consist of 20 layers in total, the covariance matrix for each degree and order is a 20×20 matrix. Finally, we iteratively find the viscosity solutions based on the simulated noisy tomography models by fitting the synthetic geoid. The deviation of the viscosity solutions from the 'true' viscosity indicates how strongly the solutions are affected by uncertainties in the tomography models.

The geoid error propagated from the tomography covariance matrix is substantially larger than the uncertainty in the observed geoid currently available from various satellite tracking data, as shown in Fig. 4(a). The predicted geoid errors from the covariance of the seismic tomography models considering the various viscosity models (referred as M1–M5 shown in Fig. 5) are also included. In addition, in order to figure out how the DSF affects the viscosity solutions, we perform similar simulations using noisy DSF's randomly generated within the bounds shown in Fig. 4(b).

Fig. 5 shows the histogram of the viscosity solutions simulated for various cases of the viscosity models (M1–M5). The distribution shows biases as well as scatters among the viscosity solutions. In some cases such as in M2 and M3, the biases are greater than the scatters in the solutions. In addition, the viscosity solutions depend on the spectral band of the geoid used in the optimization. Fig. 6 shows the distribution of the viscosity solutions under the random errors in DSF, but using the mean tomography model. Unlike the uncertainty in the tomography model, the uncertainty in DSF does not yield biases in the viscosity solutions. The DSF scales the amplitude of density variation derived from tomography models in each layer. The random errors in the amplitude of density variation do not cause biases in the viscosity solution. On the contrary, the errors in tomography models may decrease the correlation between the density structure and the observed geoid as well as yield errors in the amplitude of density variations. They essentially cause biases in the viscosity solutions. Because of these biases, the amplitude of the computed geoid tends to be under-predicted in general.

Various error covariance models (referred as E1–E6) scaled from E4 by 0.1^2 for E1, 0.3^2 for E2, 0.5^2 for E3, 1.5^2 for E5, and 2.0^2 for

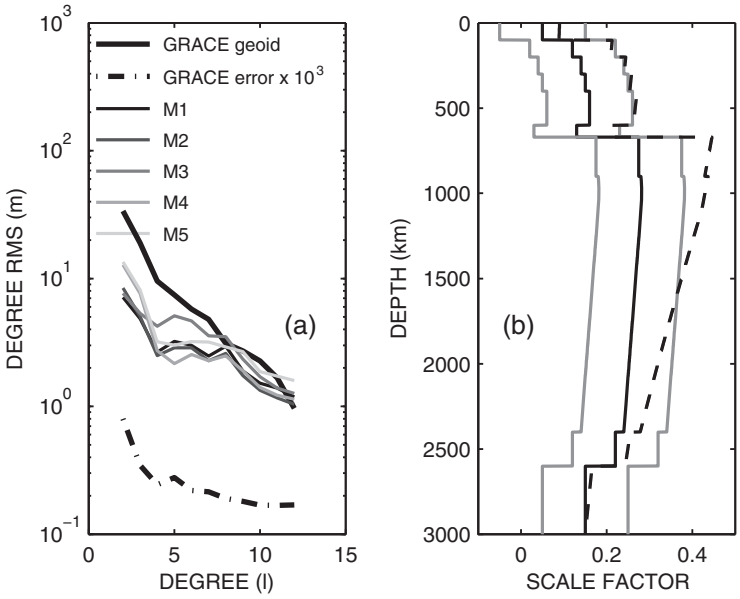

Fig. 4. (a) Degree RMS of GRACE geoid (thick black solid), GRACE geoid error (black dot-dashed), and the geoid model error caused by uncertainty in the current seismic tomography models with various viscosity models (thin solid lines). The viscosity structures for various models (M1–M5) are shown in Fig. 5. (b) The reference DSF (solid-black) and the upper and lower bounds (solid gray) used to simulate the effect of the uncertainty in DSF. The dashed back line indicates the adjusted DSF delineated by the TLS approach to (see the details in Section 6).

E6 are also tested, where E4 denotes the empirical error covariance determined from six sample tomography models. Fig. 7 shows the histogram of the viscosity solutions using the noisy tomography models with various noise levels (E1–E6), but with a fixed viscosity model, M3, and a fixed DSF, DSF6. The larger the uncertainty in the tomography model, the larger the biases in the viscosity solutions. For very conservative uncertainty levels such as E1 and E2, we can obtain the viscosity solution with high fidelity. For the most likely level of uncertainty, E4, the transition zone viscosity tends to be under-estimated from the low degree components of the geoid observations while it is likely to be over-estimated from the high degree bands such as $l = 6–12$ and $l = 8–12$.

5. Total least squares accounting for variable uncertainty in seismic tomography models

The determination of the viscosity structure of the mantle from the geoid observation at the surface is difficult due to not only its non-linear nature but also the uncertainty in the inherent model parameters such as density anomalies. Various analyses including King (1995), Čadek et al. (1998), and Soldati et al. (2009) are based on the error (misfit) norm constructed in the least square sense. It seeks for the solution that minimizes the deviation from the geoid observations. However, the errors in seismic models and the conversion from velocity to density variations were not con-

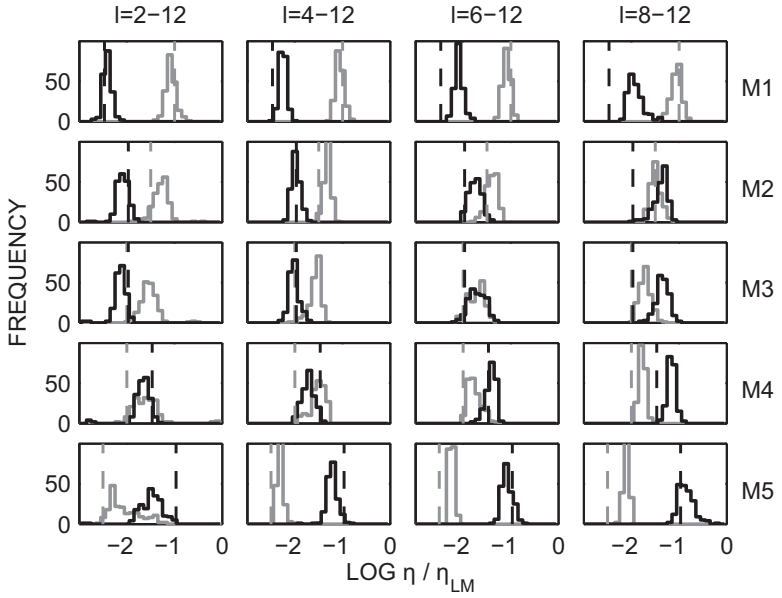

Fig. 5. Distribution of the viscosity solutions and the 'true' viscosity used in the simulations with noisy tomography models. Multiple tomography models are randomly generated with the covariance matrix determined from six tomography models. The transition zone viscosity η_{TZ} (black) and upper mantle viscosity η_{UM} (gray) are estimated from a total of 200 noisy tomography models and from the same synthetic geoid. The rows show the simulations for various viscosity structures (M1–M5). The dashed lines indicate the 'true' viscosity.

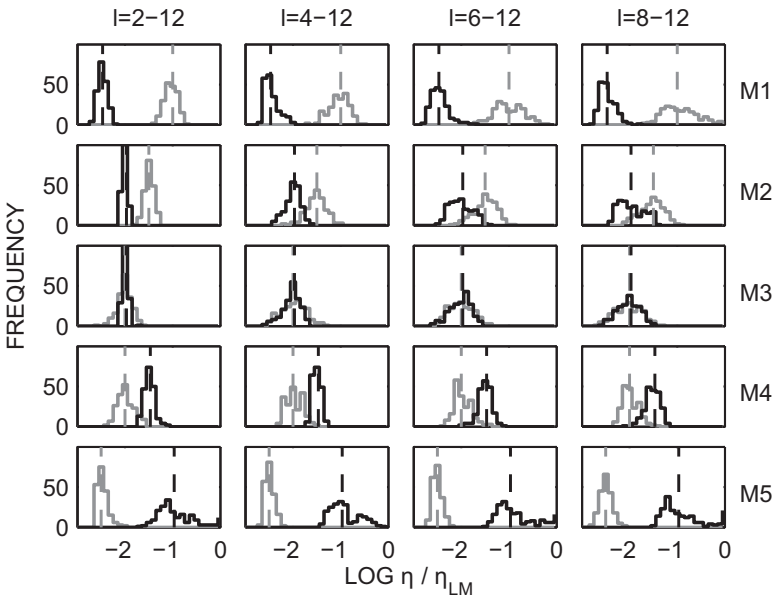

Fig. 6. The same as Fig. 5, but using randomly generated DSF's within the bounds shown in Fig. 4(b) and with the mean tomography model.

sidered explicitly. Just as discussed in Tarantola and Valette (1982) extensively, we have to consider the error in the model. Here we account for the inherent uncertainty in the density model as well as the observational noise (which, in our case, is comparatively negligible) using the so-called TLS error norm. We highlight the importance of using such an alternative error norm that requires the covariance of the seismic tomography model to find the radial viscosity structure.

With the objective to derive the explicit form of the new misfit function in this section, we start from the discrete equivalent of Eq. (1) as follows:

$$N^{lm} = \frac{3}{2l+1}\frac{1}{\bar{\rho}}\sum_{i=1}^{n}\delta\rho_i^{lm}G_i^l\Delta r_i = \frac{3}{2l+1}\frac{1}{\bar{\rho}}\sum_{i=1}^{n}\delta v_i^{lm}\zeta_i\rho_i G_i^l\Delta r_i, \tag{4}$$

where $\delta\rho_i^{lm}$, δv_i^{lm}, ζ_i, ρ_i, Δr_i are the density anomaly, the seismic velocity anomaly, the DSF, the mean density (from the PREM density model), and the thickness of each spherical shell, respectively, at depth i. The number of the spherical layers is n. Eq. (4) is then expressed into a matrix form at each degree l as

$$\mathbf{N}^l = \mathbf{A}^l\mathbf{B}^l\mathbf{G}^l = \mathbf{A}^l\mathbf{X}^l, \tag{5}$$

where $\mathbf{N}^l$ is a vector containing the $2l+1$ spherical harmonic coefficients of the model geoid at degree l, $\mathbf{A}^l$ is a $(2l+1)\times n$ matrix containing the spherical harmonic coefficients of seismic velocity anomaly at degree l, δv_i^{lm}, from a tomography model, $\mathbf{B}^l$ is a $n\times n$ diagonal matrix whose elements consist of $\frac{3}{2l+1}\frac{1}{\bar{\rho}}\zeta_i\rho_i\Delta r_i$ including the DSF and the thickness of the i-th layer, and $\mathbf{G}^l$ is a $n\times 1$ vector containing the geoid kernel at degree l, which is a non-linear function of (relative) mantle viscosity structure. We introduced a vector $\mathbf{X}^l$ for $\mathbf{B}^l\mathbf{G}^l$. For a spectral band from $l_{\min}$ to $l_{\max}$, we expand and rearrange Eq. (5) into a bigger matrix form as

$$\mathbf{N} = \mathbf{AX}, \quad \text{i.e.,} \quad \begin{pmatrix} \mathbf{N}^{l_{\min}} \\ \mathbf{N}^{l_{\min}+1} \\ \vdots \\ \mathbf{N}^{l_{\max}} \end{pmatrix} = \begin{pmatrix} \mathbf{A}^{l_{\min}} & 0 & 0 & 0 \\ 0 & \mathbf{A}^{l_{\min}+1} & 0 & 0 \\ & & \ddots & \\ 0 & 0 & 0 & \mathbf{A}^{l_{\max}} \end{pmatrix} \begin{pmatrix} \mathbf{X}^{l_{\min}} \\ \mathbf{X}^{l_{\min}+1} \\ \vdots \\ \mathbf{X}^{l_{\max}} \end{pmatrix}. \tag{6}$$

It shows a linear relationship between the geoid, **N**, and the 'effect' of mantle viscosity, **X**, that is a non-linear function of our parameter viscosity η, i.e., $\mathbf{X}(\eta)$.

Let **Y** be a vector of the geoid observation. The TLS method considers the error in the model constant such as $\mathbf{E}_A$ in addition to data noise $\mathbf{E}_Y$. The system of equations such as $\mathbf{Y}-\mathbf{E}_Y=(\mathbf{A}-\mathbf{E}_A)\mathbf{X}$

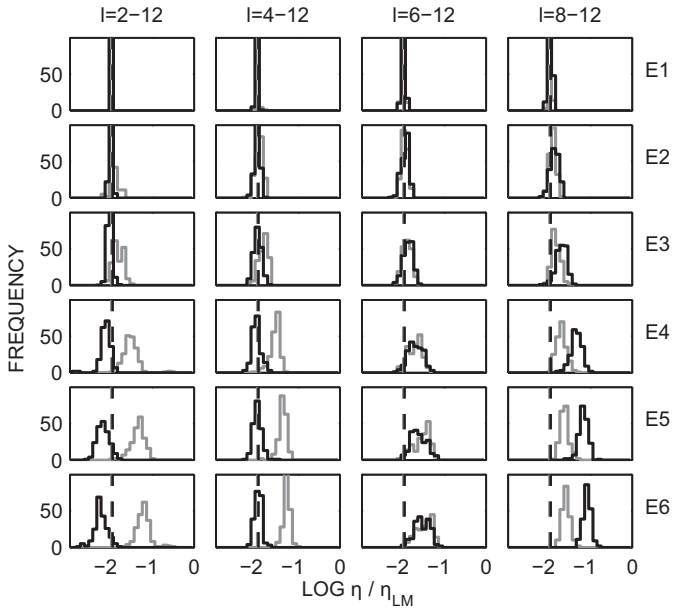

Fig. 7. The same as Fig. 5 but with various error levels in tomography models, while keeping the M3 viscosity model. The error covariance models referred as E1–E6 are scaled from E4 by 0.1^2 for E1, 0.3^2 for E2, 0.5^2 for E3, 1.5^2 for E5, and 2.0^2 for E6, where E4 denotes the empirical error covariance determined from six sample tomography models.

is a fundamental form of TLS (Van Huffel and Vandewalle, 1991). As mentioned previously, in the mantle viscosity problem with the currently available satellite data, the error caused by the model parameter, i.e., $\mathbf{E}_A\mathbf{X}$, is substantially greater than $\mathbf{E}_Y$.

The element-wise weighted total least squares (EW-TLS) defines the error norm (cost function) as a weighted norm of the residuals when $\mathbf{E}_A$ and $\mathbf{E}_Y$ are independent (De Moor, 1993; Markovsky et al., 2006). Define $\mathbf{D}=[\mathbf{A}\,\mathbf{Y}]$ and $\mathbf{E}=[\mathbf{E}_A\,\mathbf{E}_Y]$. Then, the system of equations becomes $[\mathbf{D}-\mathbf{E}]\begin{bmatrix}\mathbf{X}\\-\mathbf{I}\end{bmatrix}=0$. Let $\mathbf{e}_j{}^T$ be the j-th row of $\mathbf{E}$, i.e., $\mathbf{E}^T:=[\mathbf{E}_1\cdots\mathbf{E}_k]$. Just like the cost function of the usual LS method is a (vector) norm of $\mathbf{E}_Y$, the cost (misfit) function to be minimized in the presence of errors in both model and observation is a (Frobenius) norm of $\mathbf{E}$ defined as

$$f_0(\mathbf{X}):=\sum_{j=1}^{k} f_j(\mathbf{X})=\sum_{j=1}^{k}\mathbf{e}_j^T\mathbf{V}_j^{-1}\mathbf{e}_j, \tag{7}$$

where $\mathbf{V}_j$ is the covariance matrix corresponding the j-th row vector of the matrix $\mathbf{D}$. Following Markovsky et al. (2006), we first minimize the cost function analytically over the error $\mathbf{E}$ and then the cost function can be rewritten as

$$\begin{aligned} f_0(\mathbf{X}) &= \min_{\mathbf{E}}\sum_{j=1}^{k}\mathbf{e}_j^T\mathbf{V}_j^{-1}\mathbf{e}_j \quad \text{subject to} \quad (\mathbf{D}-\mathbf{E})\tilde{\mathbf{X}} \\ &= 0 \text{ and } \tilde{\mathbf{X}}=\begin{bmatrix}\mathbf{X}\\-\mathbf{I}\end{bmatrix}. \end{aligned} \tag{8}$$

Equivalently, one can work with a set of k independent equations given as

$$f_j(\mathbf{X})=\min_{\mathbf{e}_j}\ \mathbf{e}_j\mathbf{V}_j{}^{-1}\mathbf{e}_j \quad \text{subject to} \quad \tilde{\mathbf{X}}^T\mathbf{e}_j=r_j, \quad j=1,\ldots,k, \tag{9}$$

where the residual vector is defined as

$$\mathbf{R}:=-\mathbf{D}\tilde{\mathbf{X}}=\mathbf{Y}-\mathbf{A}\mathbf{X}, \quad \text{i.e.} \quad \mathbf{R}^T(\mathbf{X})=[r_1(\mathbf{X})\cdots r_k(\mathbf{X})]. \tag{10}$$

The functions $f_j(\mathbf{X})$ are analytically solved with respect to the vector $\mathbf{e}_j$ by introducing the Lagrange multiplier. As a result, (also found in Markovsky et al. (2006)), the solution of Eq. (8) is written explicitly as

$$f_0(\mathbf{X})=\sum_{j=1}^{k}\frac{r_j(\mathbf{X})^2}{(\tilde{\mathbf{X}}^T\mathbf{V}_j\tilde{\mathbf{X}})}. \tag{11}$$

In summary, the cost function to be minimized in the TLS framework is the sum of the squared residuals weighted by the inverse of the (co)variance of the residuals, where $var(r_i(\mathbf{X}))=\tilde{\mathbf{X}}^T\mathbf{V}_j\tilde{\mathbf{X}}$.

Since the vector $\mathbf{X}$ contains the geoid kernel that is a non-linear function of the viscosity structure for our problem, for example, we modify Eq. (11) by introducing the viscosity parameter vector $\mathbf{h}$, where $h^T=[\eta_1,\cdots,\eta_p]$. Let $\mathbf{V}_j^A$ be the covariance matrix of the j-th row of the matrix $\mathbf{A}$ and V_j^Y be the variance of the j-th measurement in $\mathbf{Y}$. The TLS cost function is expressed with the model parameter $\mathbf{h}$ as follows:

$$\psi_{TLS}(\mathbf{h})=\sum_{j=1}^{k}\frac{r_j(\mathbf{h})^2}{\mathbf{X}(\mathbf{h})^T\mathbf{V}_j^A\mathbf{X}(\mathbf{h})+V_j^Y}. \tag{12}$$

In Eq. (6), the j-th element N_j of the vector $\mathbf{N}$ is given by $N_j=\mathbf{A}_j^T\mathbf{X}=\mathbf{X}^T\mathbf{A}_j$, where $\mathbf{A}_j$ is a row vector of matrix $\mathbf{A}$. When the covariance matrix of a row vector $\mathbf{A}_j$ is V_j^A, the covariance of N_j is given by $cov(N_j)=\mathbf{X}^T\mathbf{V}_j^A\mathbf{X}$. It indicates that the term $\mathbf{X}(\mathbf{h})^T\mathbf{V}_j^A\mathbf{X}(\mathbf{h})$ in Eq. (12) is the same as the error variance propagated from the error covariance of the tomography model to the geoid. Therefore, the TLS cost function is the sum of the squared residuals weighted by the error variances of the geoid measurement and the error variance propagated from the covariance of the tomography model. In comparison with the LS cost function given in Eq. (3), we re-write Eq. (12) in terms of degree and order explicitly, as follows:

$$\psi_{TLS}(\mathbf{h})=\sum_{l=l_{\min}}^{l_{\max}}\sum_{m=-l}^{l}\frac{\left\{N_{lm}^{\text{obs}}-N_{lm}^{\text{mod}}(\mathbf{h})\right\}^2}{\mathbf{K}_l(\mathbf{h})^T\mathbf{V}_{lm}^A\mathbf{K}_l(\mathbf{h})+V_{lm}^Y}, \tag{13}$$

where $\mathbf{K}_l$ is a vector including the geoid kernels at degree l and density-velocity conversion factors, V_{lm}^A is the covariance matrix of seismic tomography at degree l and order m, and V_{lm}^Y is the geoid noise variance at degree l and order m.

The covariance matrix for the seismic tomography model we use does not yield any correlation between spherical harmonic coefficients of different degree and order. However, the coefficients in various layers are correlated. A full covariance matrix for all coefficients in all layers is not typically provided with the tomography model estimates. With this caveat, our analysis is based on the empirical covariance computed from six sample tomography models. As shown in Fig. 4, the error variance of GRACE measurement is much smaller than the error variance propagated from the covariance of the tomography model. In the weight term $\mathbf{K}_l(\mathbf{h})^T\mathbf{V}_{lm}^A\mathbf{K}_l(\mathbf{h})+V_{lm}^Y$ of Eq. (13), the error of GRACE measurements, V_{lm}^Y, is negligible in practice. For the usual LS solutions, the denominator in Eq. (13) is assumed to be a constant, which results in Eq. (3). In the following section, we present the viscosity estimation based on the alternative cost function given in Eq. (13).

6. Viscosity structure from TLS

Fig. 8 shows the histograms of the viscosity solutions, just like Fig. 5, but based on the TLS misfit function. Compared to the LS results, the biases in the TLS solutions are much smaller. For M1 and M5 viscosity models, the solutions for the more viscous layer (upper mantle for M1, transition zone for M5) are more scattered. This indicates that the geoid is less sensitive to the more viscous layer when the viscosity difference between two layers is relatively large and when the uncertainty in the seismic tomography model is incorporated. An increased uncertainty in the tomography model leads a gradual increase in the scatters of the TLS solutions as shown in Fig. 9, while it causes an increase in the biases of the LS solutions (shown in Fig. 7).

We apply the TLS method to the viscosity optimization using actual GRACE geoid measurements. The viscosity solutions that minimize the TLS misfit function given in Eq. (13) are found from randomly-generated noisy tomography models and with various DSF's. This provides a range of plausible solutions from the actual data. The reference DSF, DSF6, is scaled by the factors 1.0, 1.2, 1.4, 1.6, 1.8 and 2. Fig. 10 shows the histograms of the TLS solutions from various spectral bands and factors. For DSF6 (denoted by '×1.0' in Fig. 10), the viscosity solutions for $l=2$–12 are comparatively localized, but the solutions from the other bands are more spread out and different from the one for $l=2$–12. When the DSF is amplified, the viscosity solutions from the higher degree bands become more localized and more similar. The geoid in the higher degree bands is affected by density anomalies mostly in the shallower layers. The viscosity solutions from the higher degree bands suggest a larger ratio of density to seismic velocity anomaly than DSF6 or an underestimated velocity anomaly in the shallower layers.

The DSF6 is adjusted allowing larger scale factors for the shallow layers, as shown in Fig. 4(b). The adjusted DSF is created by multiplying to DSF6 with a factor linearly varying from 1.0 at the CMB to 1.8 at the Earth's surface. With this change, the viscosity solutions based on the TLS cost function are better localized for all spectral bands (Fig. 11(a)). In addition, unlike the solutions based on the LS cost function shown in Fig. 11(b), the biases (or inconsis-

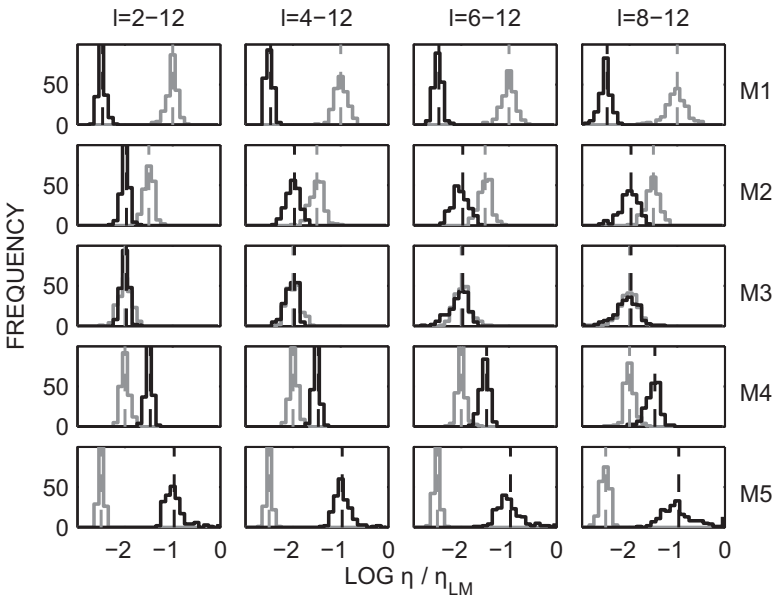

Fig. 8. As for Fig. 5, but from the TLS method.

tency) dependent on the spectral degree of the observations are not substantial in the TLS solutions. Fig. 11(c) and (d) show examples of the LS simulations using the viscosity model ($\eta_{UM}/\eta_{LM} = 10^{-2.3}$, $\eta_{TZ}/\eta_{LM} = 10^{-2.1}$) that can be delineated from the TLS solutions and randomly generated tomography models. The simulations with the E4 covariance, presented in Fig. 11(c), show less bias than the results from the actual data analysis in Fig. 11(b). The results with increased error level such as the E6 covariance present more similar patterns to the bias in the viscosity solution. It may be possible that the error estimates based on six sample tomography models are smaller than the actual error level of seismic tomography.

Fig. 12 presents the best-fitting viscosity profiles derived from six tomography models using TLS and the adjusted DSF. Compared with Fig. 3 showing the LS solutions, the dependence of the viscosity solutions on the spectral band is reduced. In general, the difference of the viscosity in transition zone and upper mantle from the TLS method is smaller than the difference found with the LS method.

7. Alternative radial parameterizations

Forte et al. (1993) and Mitrovica and Forte (2004) present a best-fit viscosity model which includes a thin low-viscosity zone at the bottom of the upper mantle. We modified the radial viscosity parameters by adding such thin (70 km) layer below the transition zone. Now, three relative viscosity parameters in the upper mantle (with respect to the lower mantle viscosity) are to be determined

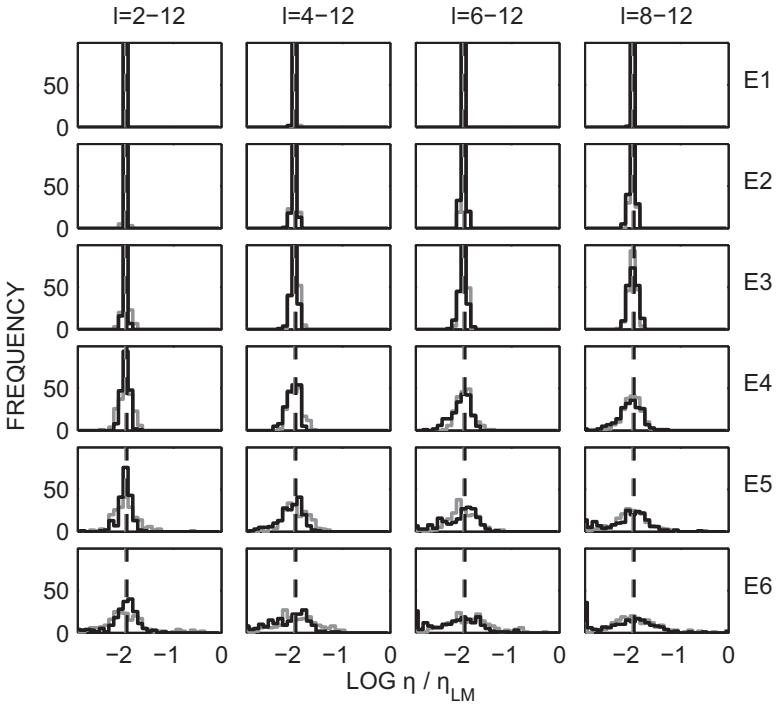

Fig. 9. As for Fig. 7, but from the TLS method.

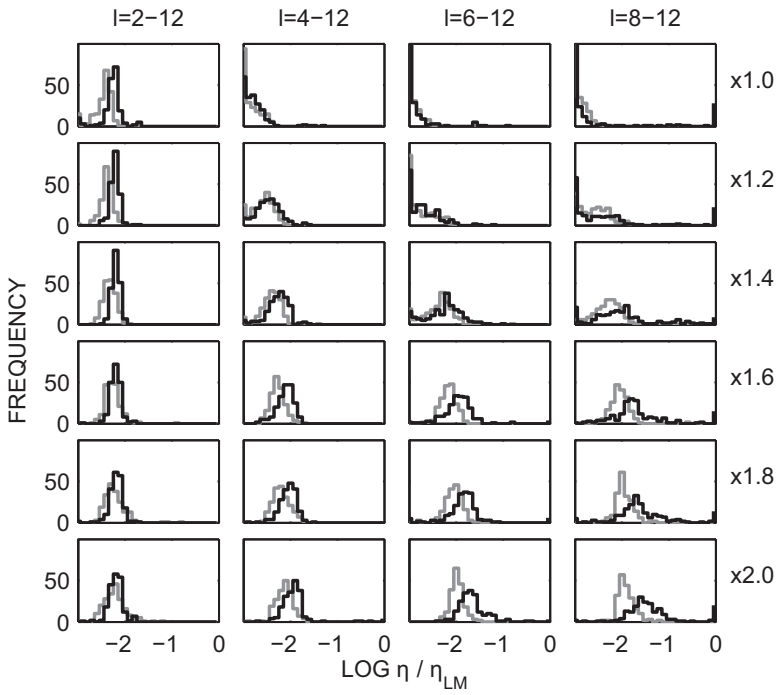

Fig. 10. Distribution of the TLS solutions computed for the actual GRACE geoid considering various cases of DSF. The reference DSF6 was multiplied by factors of 1.0, 1.2, 1.4, 1.6, 1.8 and 2.0 (from upper panels to lower panels).

using the LS and TLS methods. As discussed previously, Fig. 13(a) and (e) shows the LS and TLS results for the case of two viscosity layers in the upper mantle, respectively. It highlights that the lower viscosity in the transition zone, which can be inferred from the LS results, is not a robust feature and does not appear when we account for the uncertainty in the seismic tomography models in the viscosity inversion process. Fig. 13(b) and (f) present the respective LS and TLS solutions for the model with three viscosity layers in the upper mantle. The LS solutions indeed indicate a thin layer with extremely low viscosity. However, the viscosity in the transition zone increases, so that both effects are compensated resulting in a similar effect on the geoid as in the case of (a). However, such a feature is less pronounced in the TLS solutions which delineate two sets of possible viscosity structures: one is only slightly different from the two layer viscosity model shown in (e) and the other one indicates a thin layer at the bottom of the upper mantle, with viscosity lower than in the transition zone, but not as low as found with the LS method.

King (1995) presents a class of viscosity models characterized in general by a high-viscosity transition zone and a pronounced

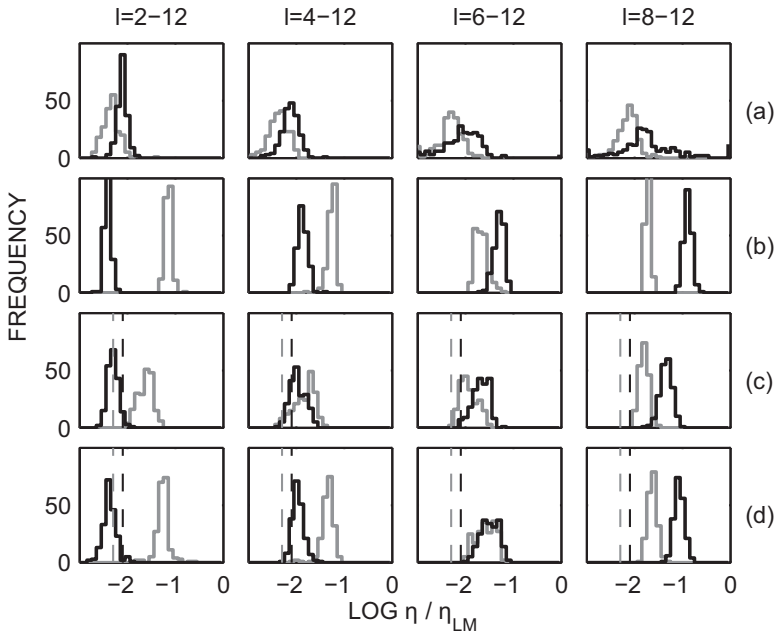

Fig. 11. Distribution of the viscosity solutions based on the adjusted DSF and the misfit functions of TLS (a) and LS (b) obtained from the GRACE geoid observation. (c) The distributions of the LS solutions from the synthetic geoid with the viscosity model denoted by the dashed lines and with the tomography model error covariance E4 (c) and E6 (d). The simulations in (c) and (d) shows a pattern of bias similar to the actual analysis for the LS solutions in (b).

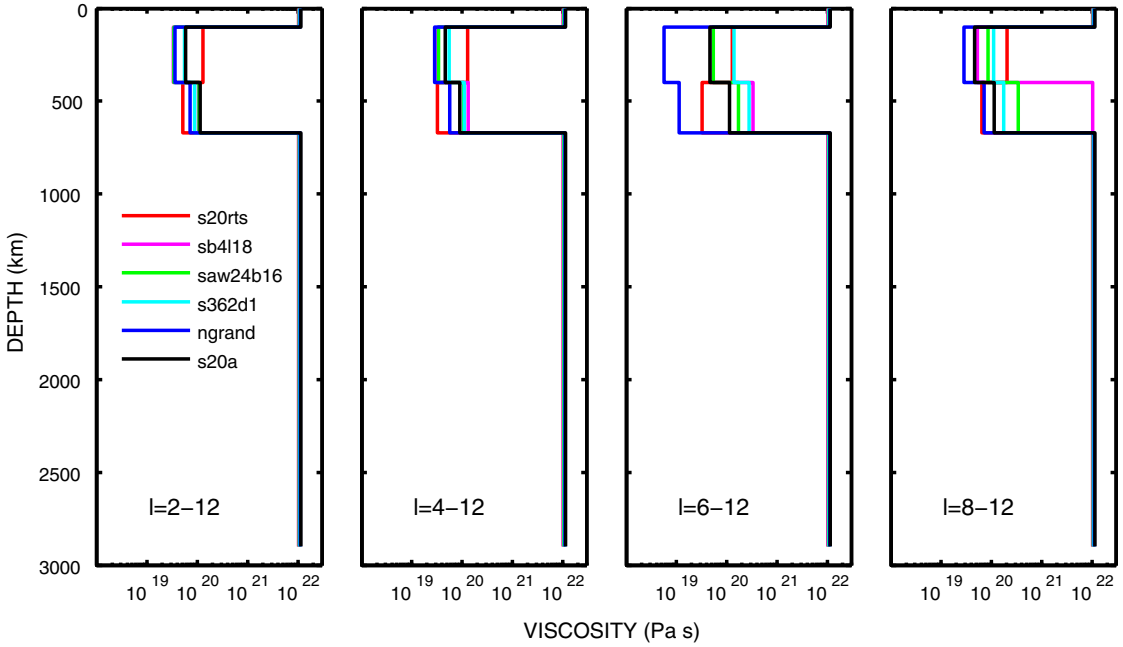

Fig. 12. Best-fitting viscosity profiles estimated with six tomography models based on the TLS approach and using the adjusted DSF.

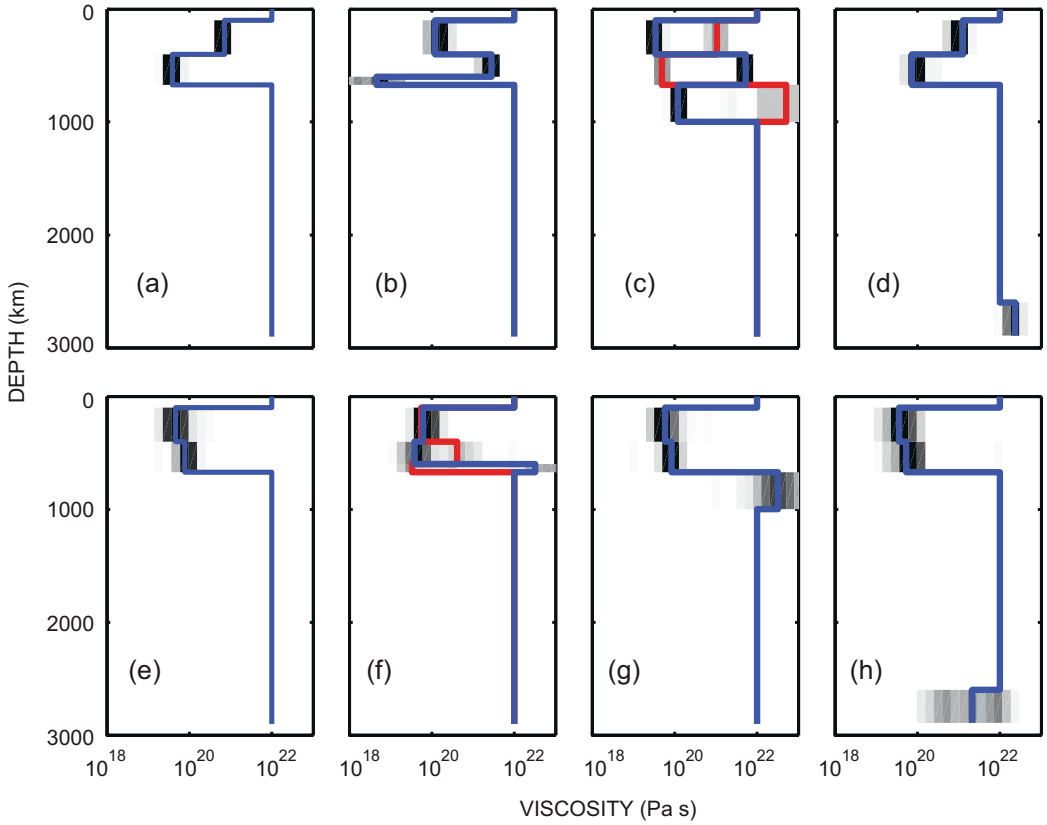

Fig. 13. Distribution of the viscosity solutions based on LS ((a)–(d)) and TLS ((e)–(h)) for the geoid observations (l = 2–12), the adjusted DSF and the mean tomography model for various radial parameterizations: a four-layer model ((a) and (e)), a five-layer model including a thin layer at the bottom of transition zone ((b) and (f)), a five-layer model including a layer from the 670-km discontinuity to 1000 km ((c) and (g)), and a five-layer model including a layer extending from 2600 km to the CMB at 2891 km ((d) and (h)). The lithosphere viscosity is set to be the same as in the middle of the lower mantle. The gray shading indicates the number of the solutions derived from 200 noisy tomography models (white counts 0, black counts over 50). It also indicates the uncertainty of the viscosity solutions that can be obtained with 'noisy' tomography models from the geoid observations. The blue line represents the most plausible solution computed by taking the mean value of the viscosity solutions in each layer. Note that, for the cases of (c) and (f), the solutions were grouped into two distinct viscosity regimes implying two possible classes of the viscosity structure. In this case, the blue line only represents one group. The red line indicates the secondary solution corresponding to the other group. This comparison shows that the viscosity solutions from the usual least-squares method are systematically biased while there are robust features delineated from the new method we propose.

low-viscosity layer below the transition zone. Čadek et al. (1998) and Kido et al. (1998) suggest that the main viscosity jump occurs at a depth of about 1000 km (not at the 660 km boundary) in their whole and layered mantle flow models. Fig. 13(c) and (g) illustrate the LS and TLS solutions from the viscosity model that includes an additional layer at the depth from 670 km to 1000 km (deeper and thicker than the previous case). As shown in Fig. 13(c), two distinct viscosity structures are delineated from the LS solutions. They are similar to the two classes found by the genetic algorithm in King (1995). The first class of the LS solutions is characterized by a high viscosity transition zone and a low viscosity zone below the transition zone. The second class of the solutions is nearly the opposite, preferring a low viscosity transition zone, just the same as found in (a). On the other hand, the TLS viscosity solutions indicate consistently a transition zone with low viscosity similar to upper mantle viscosity and a bit higher viscosity below the transition zone. Indeed, the TLS solutions are more robust with the change in seismic tomography models than the LS solutions that yield two opposite structures depending on the tomography models.

Finally, we test whether geoid observations support a low-viscosity layer near the CMB. Results do not indicate a significantly lower viscosity in the additional layer below 2600 km: viscosity slightly decreases with a large variance in TLS as shown in Fig. 13(h). The geoid data are not likely able to resolve a low viscosity layer near the CMB with high fidelity.

8. Conclusion

In this work, we highlight the effect of uncertainty in the 3D density structure (from seismic tomographical velocity models) on the inference of the radial viscosity from the geoid observations. We present systematic biases in the viscosity estimates with the 'usual' least-squares method that does not account for the variable uncertainties in the model parameters that determine density heterogeneity. We then develop the total least squares (TLS) method to account for both data noise and the uncertainties in the different model parameters. Most other studies disregard the effect that model parameters defining density structure have different uncertainties and obtain the solutions by the way of minimizing the misfit to the geoid observations simply in a least squares sense. The important finding from our experiments is that differences in uncertainty in the parameters that define the density model can cause biases in the viscosity estimates, if they are not taken into account during the inversion process. The viscosity solutions tend to underestimate the magnitude of the geoid in order to minimize the cost function of the misfit between modeled and observed geoid.

Our TLS method is established by re-defining the cost function including the effect of variable uncertainty in the model parameters describing density structure as well as the data noise. The solutions turn out to be less biased, consistent, and thus robust without a dependence on the spectral bands of the geoid observations. From the actual data analysis with a simple four-layer structure (lithosphere, upper mantle, transition zone, and lower mantle) for viscosity parameterization, the TLS viscosity solutions show that the distinction between upper mantle and transition zone viscosities is not statistically significant, unlike the solutions based on the LS methods indicating lower viscosity in the transition zone. In alternative parameterizations including one more thin or thick layer below the transition zone, the TLS solutions present robust features, i.e., two orders of magnitude smaller viscosity in the upper mantle than in the lower mantle, whereas the LS solutions are biased depending on the radial parameterization and on the seismic tomography model.

Our viscosity model, however, ignores mantle compressibility, layered convection, the effect of layer thickness variation, variation of viscosity with depth within individual layers (especially the lower mantle) and the other surface observables like surface topography, plate velocity, and post-glacial rebound. An extended analysis should include other surface data and explore more realistic viscosity structures such as proposed in Steinberger and Calderwood (2006). That is, instead of constant viscosity in each layer (upper mantle, transition zone, lower mantle), one can use 'shapes' (relative variations) within each layer determined from mineral physics but vary 'absolute' viscosity values such as to optimize the TLS fit to geoid and perhaps other observables.

The uncertainty of the TLS solution heavily depends on uncertainty in tomography models. We empirically derived the error covariance matrix of the tomography model from six sample models. The computed covariance is likely to be underestimated because common seismic data must have been used for various models. We expect the TLS analysis based on a covariance matrix for the seismic tomography models rigorously derived by seismologists should help to better quantify the interior structure of the Earth by deciphering the viscosity structure and density-to-velocity relation based on surface observations such as the geoid.

Acknowledgements

This work was supported by the U.S. National Aeronautical and Space Administration program in Earth Surface and Interior and GRACE projects. The comments by an anonymous reviewer and Mark Jellinek greatly helped improve the original manuscript.

References

Becker, T.W., Boschi, L., 2002. A comparison of tomographic and geodynamic mantle models. Geochem. Geophys. Geosyst. 3, GC000168.
Čadek, O., Yuen, D.A., Čížková, H., 1998. Mantle viscosity inferred from geoid and seismic tomography by genetic algorithms: results for layered mantle flow. Phys. Chem. Earth 23, 865–872.
Dziewonski, A.M., Anderson, D.L., 1981. Preliminary reference Earth model. Phys. Earth Planet. Inter. 25, 297–356.
Dziewonski, A.M., Hager, B.H., O'Connell, R.J., 1977. Large-Scale Heterogeneities in the Lower Mantle. J. Geophys. Res. 82 (2), 239–255, doi:10.1029/JB082i002p00239.
De Moor, B., 1993. Structured total least squares and *L2* approximation problems. Linear Algebra Appl. 188-189, 163–207.
Ekström, G., Dziewonski, A.M., 1998. The unique anisotrophy of the Pacific upper mantle. Nature 394, 168–172.
Forte, A.M., Mitrovica, J.X., 1996. New inferences of mantle viscosity from joint inversion of long-wavelength mantle convection and post-glacial rebound data. Geophys. Res. Lett. 23, 1147–1150.
Forte, A.M., Peltier, R., 1991. Viscous flow models of global geophysical observables 1. Forward problems. J. Geophys. Res., 159, 96, 20,131-20.
Forte, A.M., Peltier, W.R., 1987. Plate tectonics and aspherical Earth structure: the importance of poloidal-toroidal coupling. J. Geophys. Res. 92, 3645–3679.
Forte, A. M., Dziewonski, A. M., Woodward, R. L., 1993. Aspherical structure of the mantle, tectonic plate motions, nonhydrostatic geoid, and topography of the core-mantle boundary. In: J.-L. Le Mouel, D. E. Smylie, T. Herring (Eds.), Dynamics of the Earth's Deep Interior and Earth Rotation. Am. Geophys. Union, Geophys. Monogr. Ser., 72, 135-166.
Gordon, R.G., 2000. Diffuse oceanic plate boundaries: strain rates, vertically averaged rheology, and comparisons with narrow plate boundaries and stable plate interiors. In: Richards, M., Gordon, G., van der Hilst, R.D. (Eds.), The History and Dynamics of Global Plate Motions. Geophysical Monograph 121. American Geophysical Union, p. 398.
Grand, S.P., 2002. Mantle shear-wave tomography and the fate of subducted slabs. Philos. Trans. R. Soc. Lond. A 360, 2475–2491.
Gu, Y.J., Dziewonski, A.M., Su, W.-J., Ekström, G., 2001. Models of the mantle shear velocity and discontinuities in the pattern of lateral heterogeneities. J. Geophys. Res. 106, 11169–11199.
Hager, B.H., Richards, M.A., 1989. Long-wavelength variations in Earth's geoid: physical models and dynamical implications. Philos. Trans. R. Soc. Lond. A 328, 309–327.
Hager, B.H., O'Connell, R.J., 1981. A simple global model of plate dynamics and mantle convection. J. Geophys. Res. 86, 4843–4867.
Jordan, T.H., 1978. Composition and development of the continental tectosphere. Nature 274, 544–548.

Kaban, M.K., Rogozhina, I., Trubitsyn, V., 2007. Importance of lateral viscosity variations in the whole mantle for modelling of the dynamic geoid and surface velocities. J. Geodyn. 43, 262–273.
Karato, S.I., 1993. Importance of anelasticity in the interpretation of seismic tomography. Geophys. Res. Lett. 20, 1623–1626.
Kido, M., Yuen, D.A., Čadek, O., Nakakuki, T., 1998. Mantle viscosity derived by genetic algorithm using oceanic geoid and seismic tomography for whole-mantle versus blocked-flow situations. Phys. Earth Planet. Inter. 107, 307–326.
King, S.D., 1995. Radial models of mantle viscosity: results from a generic algorithm. Geophys. J. Int. 122, 725–734.
King, S.D., Masters, G., 1992. An inversion for radial viscosity structure using seismic tomography. Geophys. Res. Lett. 19, 1551–1554.
Kogon, M.G., McNutt, M.K., 1993. Gravity field over northern Eurasia and variations in the strength of the upper mantle. Science 259, 473–479.
Masters, G., Bolton, H., Laske, G., 1999. Joint seismic tomography for p and s velocities: how pervasive are chemical anomalies in the mantle? Eos Trans. AGU 80 (17) (Spring Meet. Suppl., S14).
Markovsky, I., Rastello, M.L., Premoli, A., Kukush, A., Van Huffel, S., 2006. The element-wise weighted total least-squares problem. Comput. Stat. Data Anal. 50, 181–209.
Mégnin, C., Romanowicz, B., 2000. The shear velocity structure of the mantle from the inversion of body, surface, and higher modes waveforms. Geophys. J. Int. 143, 709–728.
Mitrovica, J.X., Forte, A.M., 2004. A new inference of mantle viscosity based upon joint inversion of convection and glacial isostatic adjustment data. Earth Planet. Sci. Lett. 225, 177–189.
Moucha, R., Forte, A.M., Mitrovica, J.X., Daradich, A., 2007. Lateral variations in mantle rheology: implications for convection related surface observables and inferred viscosity models. Geophys. J. Int. 169, 113–135.
Panasyuk, S.V., Hager, B.H., Forte, A.M., 1996. Understanding the effects of mantle compressibility on geoid kernels. Geophys. J. Int. 124, 121–133.
Paulson, A., Zhong, S., Wahr, J., 2005. Modelling post-glacial rebound with lateral viscosity variations. Geophys. J. Int. 163, 357–371.
Ricard, Y., Vigny, C., Froidevaux, C., 1989. Mantle heterogeneities, geoid, and plate motion: a Monte Carlo inversion. J. Geophys. Res. 94, 13739–13754.
Richards, M.A., Hager, B.H., 1984. Geoid anomalies in a dynamic earth. J. Geophys. Res. 89, 5987–6002.
Richards, M.A., Hager, B.H., 1989. Effects of lateral viscosity variations on geoid anomalies and topography. J. Geophys. Res. 94, 10299–10313.
Ritsema, J., van Heijst, H.J., 2000. Seismic imaging of structural heterogeneity in Earth's mantle: evidence for large-scale mantle flow. Sci. Progr. 83, 243–259.
Sato, H., Sacks, I.S., Murase, T., 1989. The use of laboratory velocity data for estimating temperature and partial melt fraction in the low-velocity zone; comparison with heat flow and electrical conductivity studies. J. Geophys. Res. 98, 9591–9603.
Simmons, N.A., Forte, A.M., Grand, S.P., 2007. Thermochemical structure and dynamics of the African superplume. Geophys. Res. Lett. 34, L02301, doi:10.1029/2006GL028009.
Soldati, G., Boshi, L., Deschamps, F., Giardini, D., 2009. Inferring radial models of mantle viscosity from gravity (GRACE) data and an evolutionary algorithm. Phys. Earth Planet. Inter. 176, 19–32.
Steinberger, B., Calderwood, A.R., 2006. Models of large-scale viscous flow in the Earth's mantle with constraints from mineral physics and surface observations. Geophys. J. Int. 167, 1461–1481.
Tapley, B., Ries, J., Bettadpur, S., Chambers, D., Cheng, M., Condi, F., Gunter, B., Kang, Z., Nagel, P., Pastor, R., Pekker, T., Poole, S., Wang, F., 2005. GGM02—an improved Earth gravity field model from GRACE. J. Geodesy, doi:10.1007/s00190-005-0480-z.
Tarantola, A., Valette, B., 1982. Generalized nonlinear inverse problems solved using the least squares criterion. Rev. Geophys. Space Phys. 20, 219–232.
Thoraval, C., Richards, M.A., 1997. The geoid constraint in global geodynamics: viscosity structure, mantle heterogeneity models and boundary conditions. Geophys. J. Int. 131, 1–8.
Tosi, N., Čadek, O., Martinec, Z., 2009. Subducted slabs and lateral viscosity variations: effects on the long-wavelength geoid. Geophys. J. Int. 179, 813–826.
Van Huffel, S., Vandewalle, J., 1991. The Total Least Squares Problem: Computational Aspects and Analysis. SIAM, Philadelphia.
Wen, L., Anderson, D.L., 1997. Layered mantle convection: a model for geoid and topography. Earth Planet. Sci. Lett. 146, 367–377.
Zhang, S., Christensen, U.R., 1993. Some effects of lateral viscosity variations on geoid and surface velocities induced by density anomalies in the mantle. Geophys. J. Int. 114, 531–547.